Natural Hazards (2021) 106:1703–1728
https://doi.org/10.1007/s11069-020-04245-9

ORIGINAL PAPER

Real-time pressure disturbance monitoring system in the Yellow Sea: pilot test during the period of March to April 2018

Myung-Seok Kim[1] · Hyunmin Eom[2] · Sung Hyup You[2] · Seung-Buhm Woo[1]

Received: 3 February 2020 / Accepted: 21 August 2020 / Published online: 11 September 2020
© Springer Nature B.V. 2020

Abstract
Until now, the meteotsunamis reported in the Yellow Sea have been caused by sudden pressure disturbances; however, no suitable monitoring system has been established for these disturbances. With the maximum available pressure data based on 89 automatic weather stations (AWS), a real-time pressure disturbance monitoring system was developed for meteotsunami disaster prevention. When a pressure disturbance calculated from a rate of pressure change exceeds 1.2 hPa/10 min at a certain AWS, the monitoring system detects the occurrence of a pressure jump that can generate meteotsunamis in the Yellow Sea. The real-time monitoring system is operated by sending a short message service to hazard areas where destructive meteotsunamis are expected to occur by monitoring the intensity of the pressure disturbance and its propagation direction. During the pilot test from March to April 2018, the monitoring system detected four pressure jump events in total, two of which caused meteotsunamis. On the two meteotsunami event dates, the monitored pressure disturbances exceeded the intensity criteria for a common pressure jump and showed similar propagation patterns with the meteotsunamis. In particular, both meteotsunami events occurred only when the pressure jump, spatially characterized as a linear or bow type, propagated at least 12 m/s. Despite the limited number of events during the pilot test, this study provides an example of a meteotsunami-monitoring system and implications for additional pressure jump conditions favorable to meteotsunami occurrence.

Keyword Meteotsunami · Pressure disturbance · Pressure jump · Real-time monitoring system · Yellow sea

Abbreviations

AWS	Automatic weather stations
AWS #1	AWS in caution zone
AWS #2	AWS in warning zone
KST	Korea standard time (UTC + 09:00)

✉ Seung-Buhm Woo
sbwoo@inha.ac.kr

[1] Department of Ocean Sciences, Inha University, Incheon 22212, Republic of Korea

[2] Marine Meteorology Division, Korea Meteorological Administration, Seoul 07062, Republic of Korea

SMS #1 Preliminary caution SMS
SMS #2 Propagation warning SMS
TG Tide gauges

1 Introduction

Unexpected meteotsunamis in the Yellow Sea cause coastal hazards (Choi et al. 2008). On March 31 in 2007, tsunami-like waves with the largest wave height of 2.5 m were observed at dawn (Kim et al. 2017). Four people died, and it created approximately 2 million US dollars in damage, which consisted of 158 flooded houses, 150 damaged ships, 20 flooded vehicles, 45,000 m^2 of fish farm loss, and flooding at nuclear power plants (Eom et al. 2012). On Sunday noon, May 4, 2008, 24 fishermen near the coast were washed away by abnormal waves (Choi and Lee 2009) that left nine dead and 15 injured. Although not quantitatively reported, on April 26, 2011, fishing boats and fish farms were damaged by resonant waves with a period of less than 20 min (Kim et al. 2019). To date, meteotsunamis, characterized by their large amplification (Rabinovich 2009), have been widely reported in the northern Adriatic Sea (Šepić et al. 2012, 2015a), Balearic islands (Gomis et al. 1993; Garcies et al. 1996; Rabinovich and Monserrat 1996, 1998; Marcos et al. 2009), northern Malta (Drago 2009), southwestern Sicily (Candela et al. 1999; Šepić et al. 2018), Nagasaki Bay (Hibiya and Kajiura 1982), northwestern Black Sea (Šepić et al. 2015b), Gulf of Finland (Pellikka et al. 2014), Atlantic coast, the Great lakes (Šepić and Rabinovich 2014; Bechle and Wu 2014; Bechle et al. 2015; Linares et al. 2016), western Australia (Pattiaratchi and Wijeratne 2014), and the central English channel (Ozsoy et al. 2016).

Hazardous meteotsunamis are the result of amplification of waves by one or more resonance mechanisms during generation, propagation, and inundation (Monserrat et al. 2006; Pattiaratchi and Wijeratne 2016). Traveling atmospheric disturbances associated with atmospheric gravity waves, pressure jumps, frontal passages, squall lines, or other types of atmospheric disturbances (Rabinovich and Monserrat 1998; Monserrat et al. 2006; Belušić et al. 2007) initially generate ocean waves with amplitudes of several centimeters in open ocean. In the propagation process, an external resonance such as Proudman resonance (Proudman 1929) or Greenspan resonance (Greenspan 1956) occurs when the speed of ocean waves propagating toward the shallow areas matches the speed of the atmospheric disturbance. Then, the sea level oscillations may be significantly amplified by internal resonance between eigen periods that are the resonant periods of the basin (Rabinovich 2009) and dominant periods of the arriving open-ocean waves. As a result, destructive meteotsunamis of up to a few meters can be observed in coastal regions and harbors (Monserrat et al. 2006).

The possibility of meteotsunami warning systems that detect abrupt atmospheric disturbances has been suggested to monitor potentially increased wave height of the meteotsunamis by several tens of centimeters to a few meters. It requires the following: (i) a proxy-based assessment by quantifying the relationship between favorable synoptic patterns and the observed meteotsunami wave height (Šepić et al. 2016; Vilibić et al. 2018), (ii) the real-time meteotsunami detection algorithm considering meteotsunami favorable conditions of pressure disturbances (Šepić et al. 2009; Šepić and Vilibić 2011), and (iii) near-term prediction for tracking spatial and temporal patterns of meteotsunamis using land-based pressure measurements and radar-measured reflectivity (Wertman et al. 2014). Despite previous studies, there was not any meteotsunami warning system for the Yellow

Sea. Most previous studies in the Yellow Sea have been focused on analyzing the causes of the reported meteotsunami events.

We have developed a real-time pressure disturbance monitoring system in the Yellow Sea. This monitoring system aims to detect the arrival time and propagation of pressure disturbance before destructive meteotsunamis reach the coast and to issue a timely warning by sending a short message service (SMS). Probabilistic meteotsunami warning is possible by monitoring the pressure disturbance, based on the reports that the meteotsunami events in the Yellow Sea were related to a sudden change of air pressure in time (Choi et al. 2008; Choi and Lee 2009; Eom et al. 2012; Kim et al. 2014) and a certain level of pressure disturbance (Kim et al. 2019). Among automatic weather stations (AWS) currently operated by the Korea Meteorological Administration (KMA), 17 AWS located on islands and 72 AWS along the coastline of the Yellow Sea (red crosses and green circles in Fig. 1) were selected as an observation system for the monitoring system. As a detection strategy of the generation and propagation of

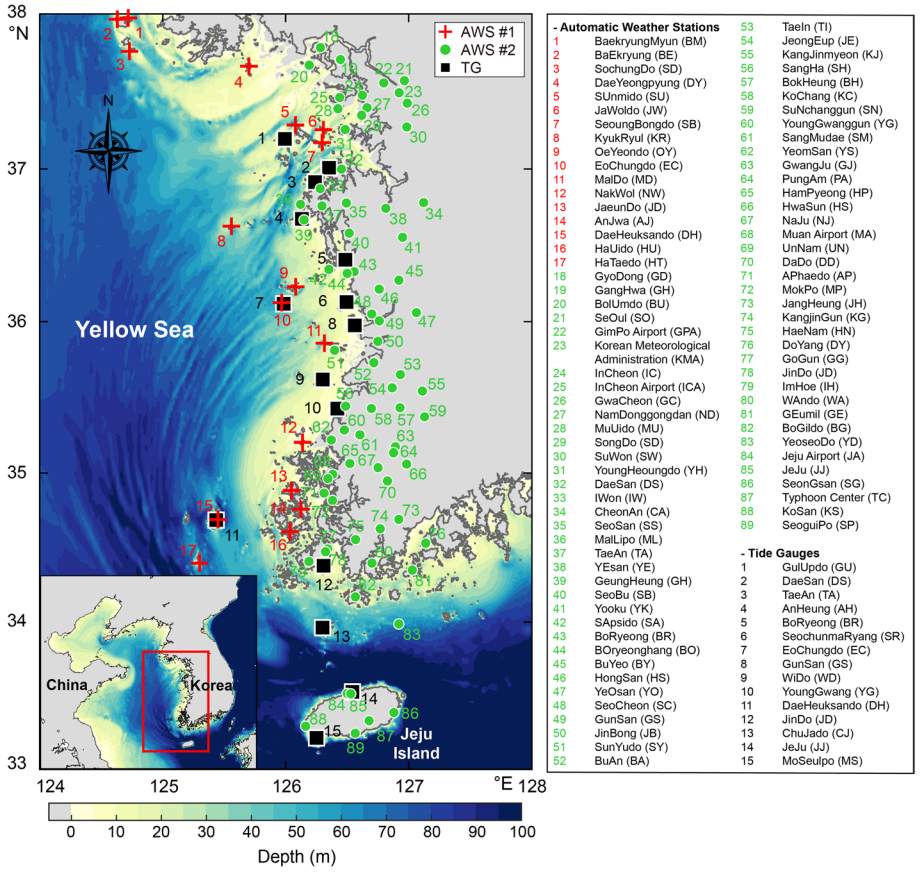


Fig. 1 Location and bathymetry of the Yellow Sea, observation stations for 89 automatic weather stations (AWS), and 15 tide gauges (TG). Red crosses and green circles indicate 17 AWS in caution zone (AWS #1) and 72 AWS in warning zone (AWS #2), respectively. Black squares represent TG. List of the stations (number, full name, and abbreviation) is given in the right column. Station numbers in the map correspond to the numbers in the column

meteotsunamis, the prototype of the meteotsunami warning systems in the Yellow Sea can be established with low cost by utilizing the existing observation system.

In this paper, the results from the pilot test of the real-time pressure disturbance monitoring system will be presented. Considering that the pressure-forced seiches frequently occurred during the Northern Hemisphere spring season (Kim et al. 2014) and that the reported meteotsunami events also occurred in the spring season, the pilot test of the monitoring system was operated during the spring season, March and April 2018. In particular, we aim to examine the practicality and accuracy of the real-time pressure disturbance monitoring system and to find common characteristics of the pressure disturbance favorable for meteotsunami development. The limitations of and recommendations for the present observation and the monitoring systems will be discussed in the last section.

2 Real-time pressure disturbance monitoring system

2.1 Observation system

Pressure data (reduced to mean sea level) is recorded at 1 min intervals by the AWS operated by the KMA. For the test run of the real-time pressure disturbance monitoring system in collaboration with the KMA, 89 AWS primarily located on an island or along the coastline were selected. To issue two levels of pressure jump warning, the 89 AWS were divided into caution zone and warning zone based on their location. Seventeen beacon AWS in the caution zone (AWS #1, red crosses in Fig. 1) located on the outermost island at each latitude monitored a pressure jump and sent preliminary caution SMS (SMS #1). Also, 72 AWS in the warning zone (AWS #2, green circles in Fig. 1) located along the west coast of the Yellow Sea detected the pressure jump propagated from the prior caution zone and sent propagation warning SMS (SMS#2). The caution zone and warning zone in the existing observation system were classified based on proximity to the mainland. It has been reported that the meteotsunamis that propagated to the mainland were more extensive and fatal than those that propagated locally to each island (Kim et al. 2019). Therefore, it was necessary to apply SMS #1 as a prior warning before SMS #2 to secure time for people to evacuate on the mainland.

During the period that the pressure jump lasted in the Yellow Sea, the temporal and spatial propagation patterns were examined by monitoring an isochrone map derived from a list of arrival times of the pressure jumps and AWS location. To verify the accuracy of the isochrone map, the propagation pattern of a rain cluster on radar, provided at 10-min intervals, was analyzed after the real-time pressure disturbance monitoring. The maximum pressure anomalies, high-frequency sea-level oscillations, and peak radar reflectivity are highly correlated in terms of arrival time and intensity (Wertman et al. 2014). To assess the occurrence and propagation of the meteotsunami once the pressure jump was detected, tide levels sampled at 1-min intervals from 15 tide gauges (TG, black squares in Fig. 1) were analyzed. The TG are operated by the Korea Hydrographic and Oceanographic Agency (KHOA).

2.2 Pressure jump detection

In 2017, the KMA used a method to detect a pressure disturbance with a range of pressure changes when establishing an initial pressure disturbance monitoring system. The detection method of a pressure jump using the range of pressure change is as follows:

- Reduction of noise in 1 min sampled raw pressure data by ensemble averaging at 10 min intervals.
- Pressure disturbance was defined as the range of ensemble averaged pressure between the real-time analysis time and the previous 60 min. Similar to the moving average process, it was calculated every 10 min with the 60-min moving time window.
- If the derived pressure disturbance exceeded 3.0 hPa/60 min, the pressure disturbance was considered as a pressure jump that could generate meteotsunamis in the Yellow Sea.

However, due to the ensemble averaging process, an abrupt pressure disturbance lasting fewer than 10 min could not be detected. Moreover, a low- or high-pressure system that falls or rises over several hours was classified as a pressure jump because the pressure disturbance was calculated from the 60 min range of pressure change.

For the test operation of the real-time pressure disturbance monitoring system in 2018, the reported problems of the previous method needed to be improved. In particular, a new method was required to detect rapid changes in raw air pressure over a short period, without classifying the large-scale pressure system as a pressure jump. Therefore, the size of the moving time window was reduced, and a pressure disturbance measured based on a rate of pressure change (Šepić et al. 2009; Šepić and Vilibić 2011) rather than a range of pressure change. The improved method for pressure jump detection is as follows:

- The raw pressure data sampled at 1-min intervals was used without any preprocessing.
- An absolute rate of pressure change over 10 min was defined as a pressure disturbance (Fig. 2). With the 10-min moving time window, each pressure disturbance was calculated at 1-min intervals.
- When a pressure disturbance exceeded 1.2 hPa/10 min, it was considered a pressure jump. The criteria for a pressure jump in the Yellow Sea was derived from the minimum absolute rate of pressure change on the reported meteotsunami events (Kim et al. 2019).

2.3 Preliminary caution SMS

An SMS #1 was sent to residents near the pressure jump detected "beacon" AWS #1. When sending SMS #1 in real time, the protocol for pressure jump caution is important. Depending on the protocol, SMS #1 can be sent too frequently or too rarely. SMS #1 was sent when a pressure jump was detected at a certain AWS #1 and the following time requirements (Fig. 2) were satisfied:

- FTP download response time ($T1$, 10 min): When operating the real-time pressure disturbance monitoring system, it was necessary to consider the delayed time for raw pressure data observed at each AWS to be sent to the KMA via the file transfer protocol (FTP) server. In some cases, although the pressure jump occurred, the pressure jump caution may have been missed due to the $T1$. Therefore, if a pressure jump was detected at the time between real-time analysis time (R) and $T1$, SMS #1 was sent.
- Time to prevent duplicate caution ($T2$, 6 h): This is the time interval specified to avoid duplicate SMS #1 for a previous pressure jump event that was already sent. We assumed T2 as the maximum time that the pressure jump could stay in the caution zone.

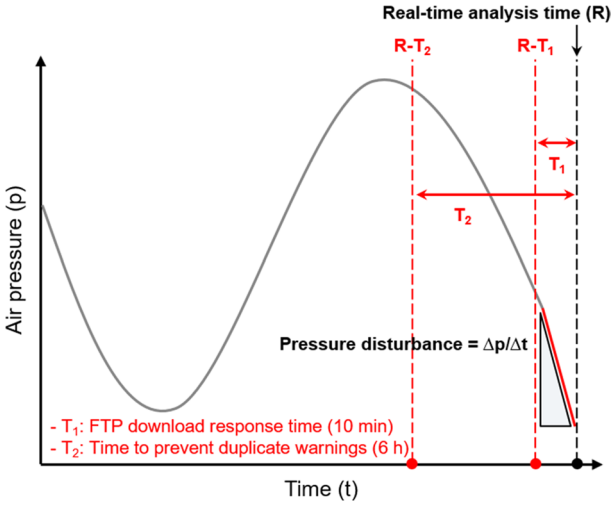


Fig. 2 Illustration of pressure disturbance (Šepić and Vilibić 2011) and time constraints of the preliminary caution short message service (SMS) in the real-time pressure jump monitoring system

- SMS #1 sending condition: An SMS #1 was sent only in case of a pressure jump was not detected at the time between $R-T2$ and $R-T1$, and a pressure jump was detected at the time between $R-T1$ and R.

2.4 Propagation warning SMS

After an SMS #1 was sent from the first AWS #1, if the propagated pressure jump was detected from at least one AWS #2; the KMA requested that the hazard-related organizations send an SMS #2 for meteotsunami disaster prevention near the AWS #2. As for the time requirements of SMS #1, $T2$ was also applied to SMS #2 to avoid the redundant warning SMS at the same AWS. To monitor the overall propagation pattern of the pressure jumps after sending SMS #2, the arrival time list accumulated over the previous 6 h from the real-time analysis time ($R-T2 \sim R$) was used. Based on the first arrival time of a specific AWS #1 where a pressure jump was detected, an isochrone map was displayed to track the propagation pattern of the pressure jump changing over time and space. The real-time monitoring system was operated every 10 min considering $T1$ and the computation time of each process.

Additional constraints were applied to reduce excessive warnings of SMS #2. First, we applied a space constraint that flags a false warning when the distance between the AWS where the pressure jump was detected in each zone exceeds 150 km. This distance was selected because the farthest distance between AWS #1 and AWS #2 does not exceed 150 km, and the average distance from AWS #1 and AWS #2 does not exceed 100 km. It is assumed that a pressure jump likely to generate meteotsunamis in the Yellow Sea propagates at a speed of at least 5 m/s. Therefore, the time constraint on pressure jump propagation from AWS #1 to AWS #2 was determined to be approximately less than 6 h. As with the space constraint, when the time constraint was not satisfied, the detected pressure jump was considered a false warning, and no SMS #2 was sent.

3 Results

3.1 Real-time pressure disturbance monitoring: caution, warning SMS, and propagation

3.1.1 The pressure jump event of 4–5 March 2018

At 18:15 KST on March 4, 2018, the first pressure jump characterized 1.9 hPa changes over 10 min (1.9 hPa/10 min) was detected at HaTaedo (17) AWS in the caution zone (Fig. 3a, e). After 5 min, an SMS #1 was sent to the area near the AWS by the real-time monitoring system. A time lag of less than 10 min can occur between the arrival time and the detection time of the pressure jump in the monitoring system. This is because raw pressure data was sampled at 1 min intervals, and the real-time monitoring system was executed every 10 min. A series of the maximum pressure jumps were detected following the first pressure jump at HT (17) AWS (red points in Fig. 3e). A rapid increase of the pressure jumps to 6.8 hPa/10 min was observed with a signal type of pressure break superposed on a low-pressure system (red line in Fig. 3a).

The maximum intensity of the pressure jump of 6.7 hPa/10 min was detected at the southernmost SeoguiPo (89) AWS in the warning zone, and an SMS #2 following an SMS #1 at HT (17) AWS was sent after 50 min (green points in Fig. 3e). Before the event, multiple pressure jumps up to 6.8 hPa/10 min lasting approximately 3 h (3/4 11:26–14:10)

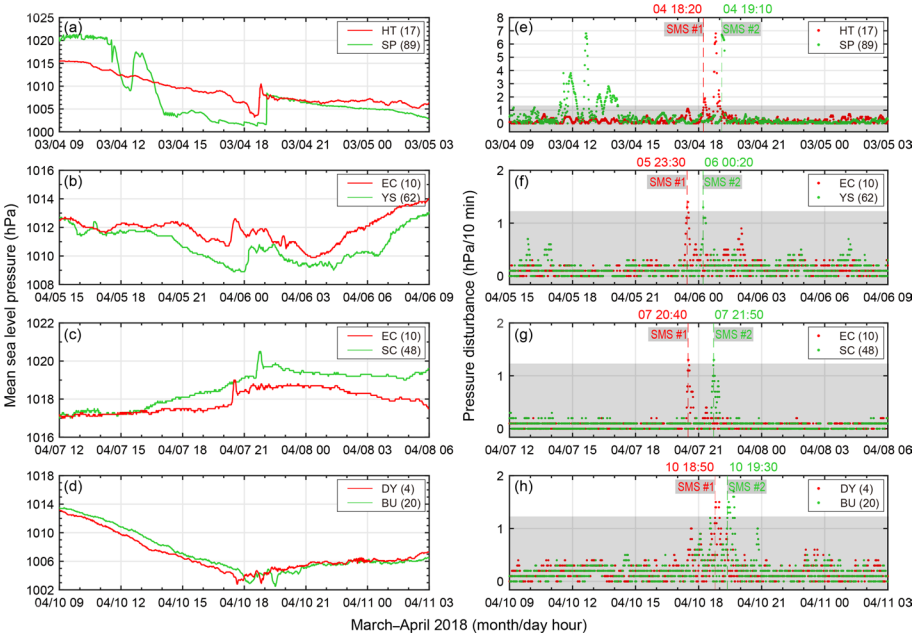


Fig. 3 Real-time pressure jump monitoring process for the preliminary caution SMS (SMS #1) and the propagation warning SMS (SMS #2): **a**–**d** mean sea level pressure at AWS #1 (red solid line) and AWS #2 (green solid line); **e**–**h** pressure disturbance (red and green points) and the first SMS sending time in the caution zone (red dashed line) and the warning zone (green dashed line); the intensity of the pressure disturbance not exceeding the limit of pressure jump (1.2 hPa/10 min) is highlighted in gray-shaded areas

Fig. 4 Monitoring results of pressure jump propagation for 4–5 March 2018 (KST): **a**, **b** isochrone map of the pressure jump during each period; red and green grid lines indicate the AWS where the first pressure jump arrived at AWS #1 and AWS #2; gray solid lines (60 min) and gray dashed lines (10 min) indicate isochrones of the pressure jump; crosses and circles indicate AWS #1 and AWS #2 where the pressure jumps were detected; the maximum intensity of the pressure jump is shown with the color of the crosses and circles; **c**, **d** rain rate on radar during pressure jump propagation; red enclosed areas are the clusters where more than 5 mm/h of rain rate was observed

were detected at the AWS. However, because no pressure jumps at AWS #1 were detected, SMS #2 was not sent. There is no AWS #1 near Jeju Island in the current observation system (Fig. 1); thus, both SMS cannot be sent when a pressure jump propagated to only Jeju Island.

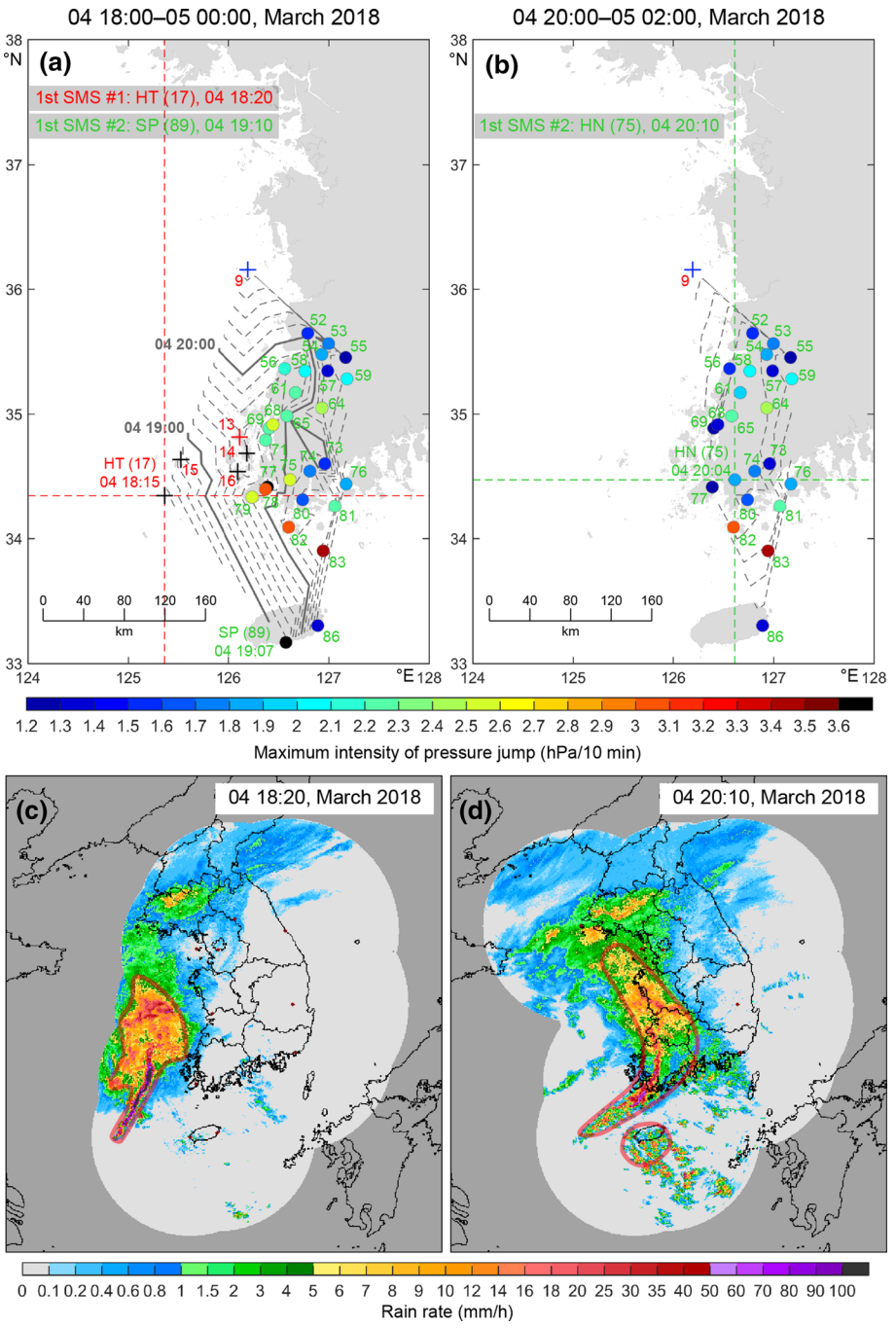
After sending the first SMS #1 and SMS #2, an isochrone map of the pressure jump was derived from an arrival time list of the pressure jumps every 6 h to monitor the temporal and spatial propagation of the pressure jump (Figs. 4, 5 and 6). AWS #1 and AWS #2 where the pressure jump occurred are marked by crosses and circles, respectively. The maximum intensity of the pressure jump during the analysis period is indicated by the color of the marker. If the AWS where first pressure jump was detected was located in the caution zone or the warning zone, it is denoted by red or green dashed lines. The gray solid lines and gray dashed lines represent the isochrone line at 1 h and 10 min intervals, respectively, based on the location and arrival time of the first pressure jump detected AWS.

Two types of propagation patterns that traveled eastward toward the southern coast and northeast toward the central coast of Korea had been observed from 18:00 KST on March 4 to 00:00 KST on March 5 (Fig. 4a) after the first detection of the pressure jump at HT (17) AWS. The spatial pattern of the rain cluster exceeding 5 mm/h was distributed similarly to the propagation pattern derived from the isochrone map of the pressure jump (red enclosed areas in Fig. 4b, d). After the first pressure jump at HT (17) AWS, pressure disturbances exceeding approximately three times of the intensity criteria for a pressure jump (3.3–6.8 hPa/10 min) were detected at DaeHeuksando (15), HaUido (16), JaeunDo (13), and AnJwa (14) AWS, in order. Around 20:00 KST on March 4, from BuAn (52) AWS to AWS on Jeju Island, multiple pressure jumps were detected with relatively attenuated intensity predominantly less than 3.0 hPa/10 min. Similar to the intensity of the pressure jumps, which drastically decreased during the propagation, the spatial scale of the rain cluster on radar also decreased sharply on land after 20:10 KST on March 4, 2018.

With AWS #1 excluded from 20:00 KST on March 4 to 02:00 KST on March 5, the first SMS #2 was sent from HaeNam (75) AWS in the warning zone (Fig. 4b). After the HN (75) AWS, the evolution of the pressure jump propagating eastward along the southern coast of Korea on land was similar to the propagation pattern of the rain cluster (Fig. 4b, d). Another pattern that propagated toward the central coast in the isochrone map and radar disappeared rapidly on land. Because additional AWS, which is located east of AWS #2, was not used for real-time monitoring, the evolution and dissipation of the pressure jump in land cannot be tracked.

3.1.2 The pressure jump event of April 5–7, 2018

On April 5–7, 2018, two different pressure jump events were successively detected. The two events had each different propagation pattern, and the spatial scales of both pressure jump events were smaller than those of the pressure event on March 4, 2018.



From 23:30 KST on April 5 to 00:20 KST on April 6, pressure jumps up to 1.9 hPa/10 min were detected at EoChungdo (10) AWS in the caution zone and propagated to YeomSan (62) AWS in the warning zone (Fig. 3b, f). As pressure jumps up to

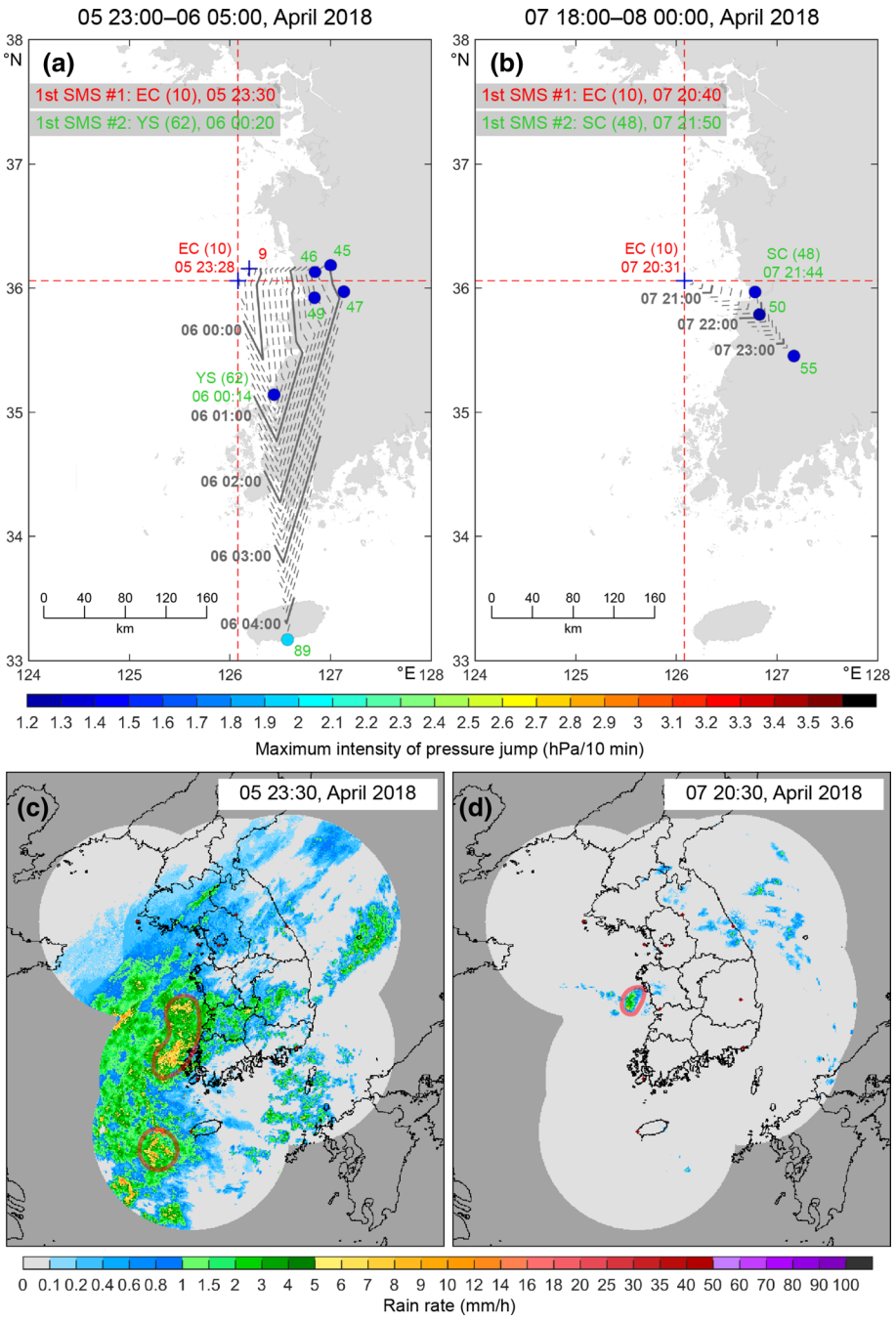


Fig. 5 As in Fig. 4, but for April 5–8, 2018 (KST)

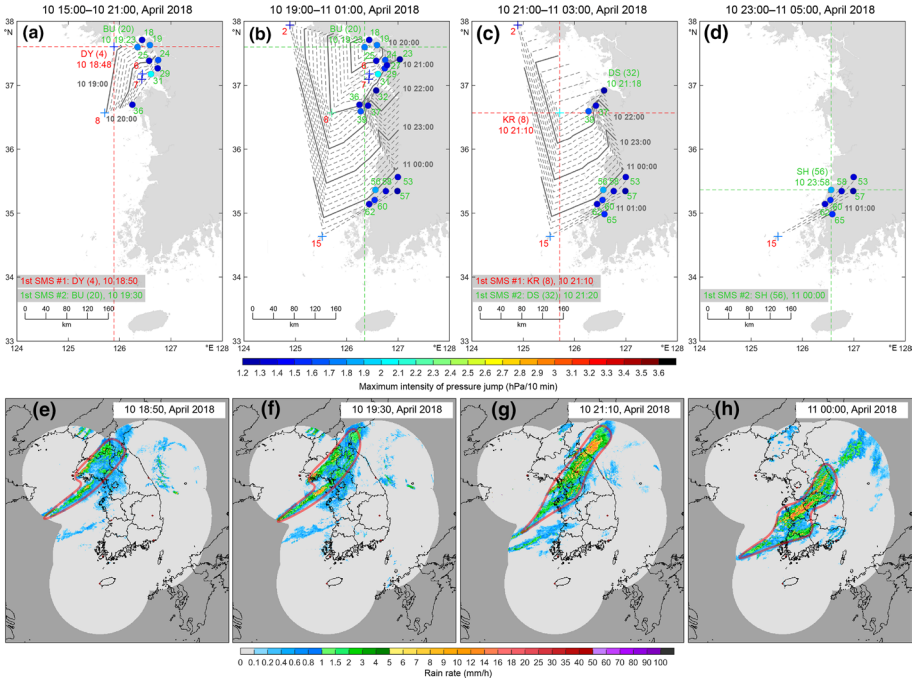


Fig. 6 As in Fig. 4, but for April 10–11, 2018 (KST)

1.3 hPa/10 min were detected at SeoCheon (48) AWS after EC (10) AWS, SMS #2 was sent at 20:40 KST on April 7 (Fig. 3c, g). Both pressure jump events barely exceeded the intensity criteria for a pressure jump. At EC (10), YS (62), and SC (48) AWS where the first SMS #1 and the following SMS #2 were sent in each zone, the pressure disturbance ranged from 1.2 hPa/10 min to 1.4 hPa/10 min (Fig. 5a, b).

From 23:28 KST on April 5 to 02:07 KST on April 6, the pressure jumps propagated eastward from EC (10) AWS to YS (62) AWS located inland (Fig. 5a). There was an approximately 4-h arrival time lag of the pressure jump at SP (89) AWS located approximately 220 km south from YS (62) AWS. No pressure jump was detected at any other AWS between the two AWS. Accordingly, additional patterns of southward propagation as well as patterns that propagate primarily eastward were shown in the isochrone map. During the period of the event, two rain clusters propagating to the coast near the central coast of Korea and propagating to SP (89) AWS were observed on radar (red enclosed areas in Fig. 5c). It is problematic that local propagation is considered an overall propagation pattern, as the current method for monitoring the propagation direction through the isochrone map uses an available arrival time list of the pressure jumps at all AWS. Therefore, it is necessary to consider additional distance and time constraints when analyzing the propagation of the pressure jumps through the isochrone map.

The pressure jump event on the April 5–6 was characterized as an event propagated with a spatial scale less than 40 km, from EC (10) AWS to KangJinmyeon (55) AWS (Fig. 5b). A local spatial scale of the rain cluster was monitored near EC (10) AWS; it propagated inland similar to the propagation pattern of the pressure jump (red enclosed areas in Fig. 5d). Unlike other pressure jump events, this was considered the

most dangerous pattern due to its intensity near the pressure jump criteria and extremely small spatial scale that made it difficult to detect.

3.1.3 The pressure jump event of 10–11 April 2018

The first SMS #1 was sent from DaeYeongpyung (4) AWS at 18:50 KST on April 10, and SMS #2 was sent from BolUmdo (20) AWS with a time lag of 40 min (Fig. 3h). From 09:00 KST on April 10 to 18:00 KST on April 10, before the pressure jumps were detected, the raw mean sea level pressure dropped from 1,013 hPa to 1,003 hPa for 9 h at DY (4) AWS and BU (20) AWS (Fig. 3d). The previous method for estimating the pressure disturbance by the range of pressure change classified even the pressure fluctuations over several hours as a pressure disturbance that can generate high-frequency sea level oscillations. However, when using the modified pressure jump detection method, these long-period pressure fluctuations (Fig. 3d) can be classified as insignificant pressure disturbances (gray shaded areas in Fig. 3h).

For approximately 6 h, from 18:48 KST on April 10 to 01:07 KST on April 11, the pressure jump propagated over the widest range of areas from the northern to the southern coast of Korea (Fig. 6a–d). The pressure jump propagated from the northern to the central coast for 2 h after 22:00 KST on April 10, but the propagation pattern near the central coast was interpolated (Fig. 6b, c) due to pressure disturbances less than the intensity criteria for a pressure jump in AWS located near the central coast (9–14 AWS #1 and 40–52 AWS #2 in Fig. 1). At AWS located near the southern coast, pressure disturbances exceeding the intensity criteria for a pressure jump were observed again at midnight on April 11 (15 AWS #1 and 53–65 AWS #2 in Fig. 6c).

Similar to the rapidly changing pressure jump as it propagated to the southern coast of Korea (Fig. 6a–d), the intensity of the linear rain cluster, which changed over time and space, propagated with the pressure jump (red enclosed areas in Fig. 6e–h). The tail of the linear rain cluster propagated southeastward and landed on the central coast after 21:00 KST on April 10, after which the intensity of the linear rain cluster fell below 5 mm/h rain rate (red enclosed areas in Fig. 6g, h). However, after midnight, the linear rain cluster near the southern coast was amplified more than the intensity decreased during the landing (red enclosed areas in Fig. 6h).

Based on the propagation of the pressure jump and the rain cluster, it was found that the initial intensity of the pressure jumps detected at AWS #1 was not maintained until it propagated to the terminal point. Therefore, to prevent accidents caused by suddenly evolving pressure jumps, it is very important to monitor the intensity of the pressure jump while tracking its propagation path.

3.2 Post-time analysis after pressure disturbance monitoring

3.2.1 Detection and first arrival time of the meteotsunami

The high-frequency sea level oscillations were examined from tide gauge data to check the occurrence of the meteotsunamis on the dates that the pressure jumps were detected. In general, meteotsunami-induced sea level oscillations are known to be related to background oscillations in the tsunami frequency band, which is less than 2 h (Monserrat et al. 2006). It has been reported that the period of pressure jump induced sea level oscillations in the Yellow Sea was less than 1 h or 2 h (Choi et al. 2008; Choi and Lee 2009; Eom et al.

2012; Kim et al. 2019). To isolate the sea level oscillations from raw tide data, tide levels were high-pass filtered with a 2 h wavelet filter (Torrence and Compo 1998), which is useful for extracting specific single events characterized as localized peaks or non-periodic peaks. The energetic oscillations in tide gauge data due to wind waves were filtered out in the sampling process.

The absolute criteria for a meteotsunami used have similar characteristics to those of the pressure jump determined based on the same intensity of the pressure disturbance for all AWS. Rabinovich and Monserrat (1996) assumed that a meteotsunami occurred when the wave height of the high-frequency sea level oscillations exceeded 30 cm and 10 cm in the Ciutadella inlet (Balearic Islands) and the Krabovaya bay (Kuril Islands). Kim et al. (2020) used amplitude criteria of 10 cm when finding the TG meteotsunami that occurred on the reported meteotsunami dates in the Yellow Sea. In this study, when the amplitude of high-frequency sea level oscillations in the meteotsunami frequency band exceeded 15 cm, it was considered that a meteotsunami occurred at the TG. The arrival time of a meteotsunami was determined as the time when the maximum amplitude at each TG was observed while exceeding the amplitude criteria for a meteotsunami in consideration of the background noise at each TG.

Through the pilot test of the monitoring system, meteotsunamis were detected on March 4, 2018, and April 10, 2018 (Fig. 7a, d). On April 5, high-frequency sea level oscillations with the maximum amplitudes of between 10 and 15 cm were observed at AnHeung (4) TG, EoChungdo (7) TG, and WiDo (9) TG near AWS where the pressure jumps had been detected (Fig. 7b). Additionally, on April 7, insignificant sea level oscillations of less than 10 cm were observed at locally limited TG (Fig. 7c).

Based on the events on March 4 and April 10 when both the pressure jumps and the meteotsunamis were detected at the same time, the real-time pressure disturbance monitoring system was examined to determine whether it is feasible to prevent destructive from meteotsunamis. In the current monitoring system, the most important point is that the first SMS #1 sending time should be faster than the arrival time of the first meteotsunami under

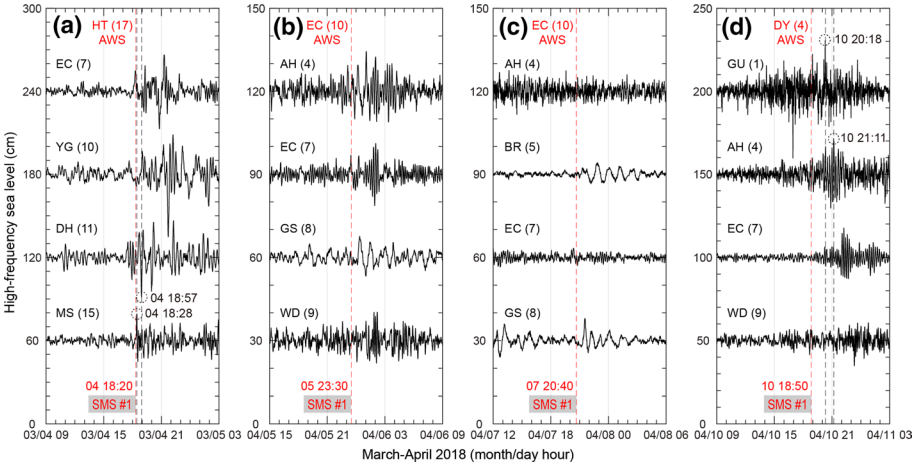


Fig. 7 Time series of the high-frequency sea level oscillations (2 h high-pass filtered) during the pressure jump events: **a** 4–5 March 2018 (KST); **b** 5–6 April 2018 (KST); **c** 7–8 April 2018 (KST); **d** 10–11 April 2018 (KST). Red dashed line indicates the first SMS #1 sending time on each pressure jump event. Gray dashed lines and gray dashed circles indicate the first and second arrival time of the meteotsunamis

any conditions. This is because people near AWS #1 who may receive SMS #1 need sufficient time to evacuate from the dangerous coast where the pressure jump induced meteotsunamis can occur.

At 18:20 KST on March 4, the first SMS #1 was sent from HT (17) AWS, and 8 min later the meteotsunami arrived at MoSeulpo (15) TG in Jeju Island (red and gray dashed lines in Fig. 7a). After sending SMS #1, up to 37 min of evacuation time was available at DaeHeuksando (11) TG when considering only the TG near the Korean Peninsula. At 18:50 KST on April 10, the first SMS #1 was sent from DY (4) AWS and 28 min later the meteotsunami arrived at GulUpdo (1) TG, located approximately 60 km southeast from the AWS (red and gray dashed lines in Fig. 7d). Based on the events when the pressure jumps and meteotsunamis were detected at the same time during the pilot test, it was confirmed that approximately 30 min of evacuation time could be allowed after sending SMS #1 in the current observation system and monitoring system.

3.2.2 Propagation of meteotsunamis

As an "early advisory" around AWS #1 where a pressure jump is detected, SMS #1 is sent to announce the source location of the first meteotsunami. After SMS #1, SMS #2 is sent for a "safety warning" of the possible human and property damage due to meteotsunamis by monitoring the pressure jump that propagates in a specific direction from the caution zone to the warning zone. Therefore, the evolution of the pressure jump monitored in real-time and the propagation patterns of the meteotsunamis analyzed after the pilot test of the monitoring system were compared from the following perspectives:

1. Was SMS #2 sent ahead of the time when a meteotsunami arrived at nearby TG?
2. Did the direction of the pressure jump derived from the monitoring system represent the direction of the meteotsunami?

In the case of SMS #1, because most AWS #1 (red crosses in Fig. 1) are located far outside the Yellow Sea relative to TG (black squares in Fig. 1), it was able to ensure sufficient evacuation time. However, most AWS #2 are located further inland or located near TG (green circles in Fig. 1). If the pressure jump does not propagate ahead of the meteotsunami, the meteotsunami will arrive at the warning zone and SMS #2 will be sent late. Therefore, it was necessary to check the difference between the arrival time of the pressure jump and the arrival time of the meteotsunamis at AWS #2 in terms of meteotsunami disaster prevention. The arrival time difference was compared based on the time when the meteotsunami arrived at a certain TG and the time when SMS #2 was sent from AWS #2 near the TG. If no AWS #2 was detected near the TG where a meteotsunami arrived, the arrival time of meteotsunamis at a certain TG and the arrival time of pressure jumps calculated from the isochrone map corresponding to the position of the TG were compared.

The arrival time difference was primarily within 10 min, except where the pressure jump propagated to regions with a depth of less than 10 m near the coast. In the event of March 4, the pressure jump was detected from ImHoe (79) AWS at 19:52 KST following SP (89) AWS (Fig. 4a), and SMS #2 was sent at 20:00 KST, and then after 7 min, the resultant meteotsunami was observed at JinDo (12) TG (Fig. 8a). Despite WD (9) TG, GunSan (8) TG, and YoungGwang (10) TG, which are distributed inside the 10.2 m depth contour line, are located relatively more east than AWS #2, the arrival time of the pressure jump was approximately 1–2 h earlier than the time when the meteotsunami

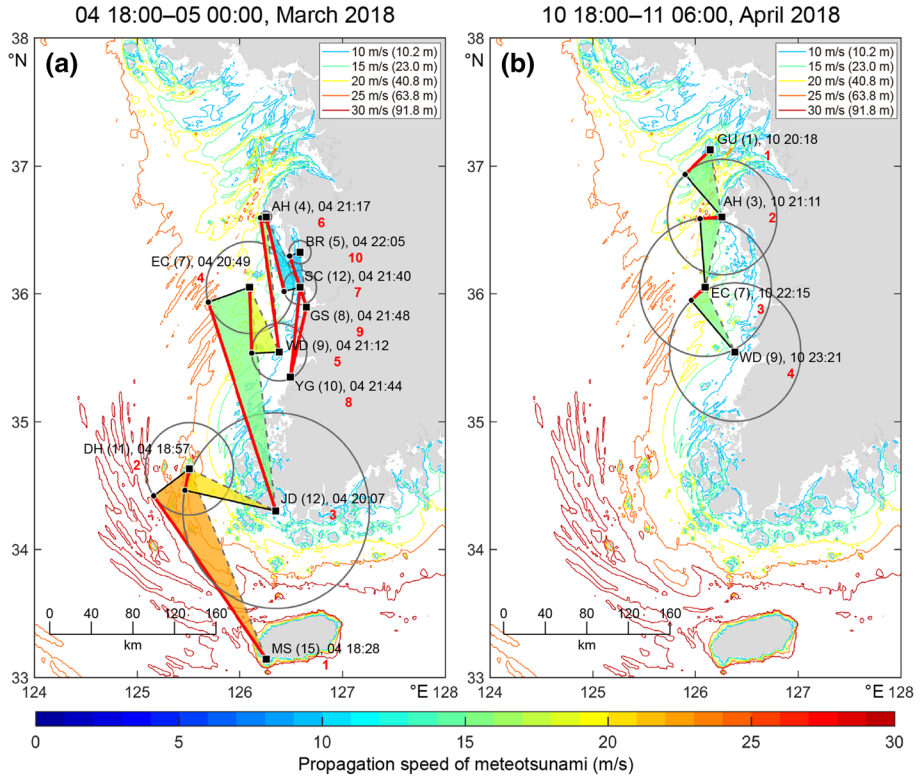


Fig. 8 Arrival time and propagation map of the meteotsunamis for: **a** March 4–5, 2018 (KST) and **b** April 10–11, 2018 (KST). Black squares mark TG where the meteotsunami arrived. Red solid lines indicate the wave crest line of meteotsunamis, and gray dashed lines mark the line connecting one TG to another. Radius of each gray circle is the distance that the meteotsunamis can propagate, and black lines denote the determined line of the radius. Black circles indicate tangent points between the wave crest line and the radius of each gray circle. Color of the triangles denotes the calculated speed of the meteotsunami in each triangle region. Bathymetric contour lines indicate the speed range of the shallow water waves (10–30 m/s) calculated from a certain range of the water depths (10.2–91.8 m)

arrived. In the event of April 10, there was almost no time lag between the arrival time of the meteotsunamis from the first GU (1) TG to the WD (9) TG (Fig. 8b) and the arrival time on the isochrone map of the pressure jump (Fig. 6b).

We assumed that a meteotsunami generally do not arrive before a pressure jump. Accordingly, if the propagated pressure jump is detected in succession at AWS #2 after the first pressure jump occurs at AWS # 1, SMS #2 can be sent before the arrival of the meteotsunami. However, when the pressure jumps and meteotsunamis are propagated with no time lag and the location of AWS #2 is more coastal than TG relative to the direction of their propagation, SMS #2 will be sent later than the actual meteotsunami arrival. This late SMS #2 can be resolved temporarily by adding a new SMS #2 transport protocol. In case that a subsequent pressure jump is detected in another AWS #1 after the first pressure jump at AWS #1, SMS #2 needs to be sent to not only AWS where the pressure jump was detected but also to AWS located along the propagation direction.

The real-time monitoring of the pressure jump propagation is performed to estimate the propagation direction of the meteotsunami in advance. The propagation direction of the pressure jumps and meteotsunamis were compared to determine if the pressure jump direction represented the actual propagation of the meteotsunami on March 4–5 and April 10–11. However, since the number of the TG (15) is much smaller than the number of the AWS (89), the isochrone map cannot be used in the same way as the pressure jump propagation method when analyzing the meteotsunami propagation. Therefore, based on the method for tracking the meteotsunami propagation even with the limited number of TG (Kim et al. 2020), the meteotsunami propagation was estimated during the same period of the pressure jump propagation.

The meteotsunami propagated from MS (15) TG to EC (7) TG (Fig. 8a) from the same source location of the pressure jump and with a similar propagation pattern of the pressure jump between 18:28 KST and 20:49 KST on March 4 (Fig. 4a). The pressure jump propagated at an average speed of 20.3 m/s from 18:00 KST to 19:00 KST on March 4, and the meteotsunami initially propagated 23.0 m/s near MS (15) TG, but as the water depth became shallower, it decelerated to 15.8 m/s near the EC (7) TG (Fig. 8a). Thus, the resonantly coupled pressure jump-meteotsunami near HT (17) AWS propagated with an approximate 0.9 Froude number (Fr), which is favorable for the occurrence of Proudman resonance. The Fr (Fr = U/c) is a ratio between pressure jump speed (U) and shallow water wave speed (c). Unlike the propagation pattern of the pressure jumps (Fig. 4a, b), which are concentrated on the southern coast of Korea, the meteotsunamis concentrated on the central coast (red solid lines in Fig. 8a) propagated perpendicular to the depth contour lines. As the intensity of the pressure jump on the central coast rapidly decreased to less than the intensity criteria for a pressure jump in the Yellow Sea, we were unable to trace where the pressure jump propagated after 21:00 KST on March 4 in the isochrone map (Fig. 4a). Instead, through the intensity and the movement of rain cluster (Fig. 4d), it was assumed that the attenuated pressure jump propagated to the southern coast and central coast like the propagation of the meteotsunami (Fig. 8a).

From 20:18 KST to 23:21 KST on April 10, the meteotsunami, which was trapped in a certain depth range, propagated to the southern coast of Korea in a direction parallel to the shoreline from GU (1) TG to the WD (9) TG (red solid lines in Fig. 8b). When comparing the arrival time of meteotsunami arrived at each TG (Fig. 8b) and the pressure jump on the isochrone map (Fig. 6a–d), there was little time difference. At this time, the pressure jump propagated from the northern coast at an average speed of 13.8 m/s from 20:00 KST to 21:00 KST on April 10 (Fig. 6a), and the meteotsunami propagated at a constant speed of 15.2–15.7 m/s (Fig. 8b). From GU (1) AWS, the pressure jump and the meteotsunami were coupled with almost no time lag and propagated with 0.9 Fr, similar to the ranges of the Fr on March 4. On March 4, the coupled pressure jump-meteotsunami propagated perpendicular to the depth contour lines and were separated near the water depth of 10.2 m (Figs. 4, 8a). However, on April 10, the coupling continued in a depth range from 23.0 to 40.8 m until the pressure jump disappeared (Figs. 6, 8b).

The propagation direction of the pressure jump derived from the real-time pressure jump monitoring system was very similar to the propagation direction of the meteotsunami calculated from the postprocessing. Therefore, it was confirmed that the approximate propagation of the meteotsunami can be detected in the pressure-based warning system. Also, except for trapped waves, which were trapped in a certain depth range and propagated at a constant speed, the speed of the meteotsunami decreased as it traveled. The decrease in propagation speed over the shallow shelf regions could have been caused by not only shallow water wave speed (Monserrat et al. 2006) but also wave interferences due to wind gusts

accompanied by the pressure disturbance (Šepić et al. 2015a), strong currents in harbors (Rabinovich 2009), and wave and tidal current interaction (Choi et al. 2014).

3.2.3 Intensity of the pressure disturbance and high-frequency sea level oscillations

Since the strength of the atmospheric disturbance (a pressure jump or a train of waves) influences the amplitude of the meteotsunamis (Šepić and Rabinovich 2014), the possibility of meteotsunami occurrence was determined by the intensity of the pressure disturbance in the current monitoring system. However, when the intensity of the pressure disturbance exceeds the pressure jump criteria, the amplitude of the high-frequency sea level oscillations does not always exceed the meteotsunami criteria (Fig. 7b, c). During the pressure jump event, the maximum amplitude of the meteotsunami relative to the maximum intensity of the pressure disturbance was compared to analyze the correlation between the intensity of the pressure disturbance and the amplitude of the sea level oscillations. The correlation was analyzed by classifying AWS-TG as five bands according to each latitude (Fig. 9) because the number of AWS-TG is different and the location where the observation position matches do not exist in the current observation system (Fig. 1).

Although it is a fairly small number of events, on each of the four pressure jump events, the maximum amplitudes of the high-frequency sea level oscillations of at least 8 cm were observed in common at the TG near the AWS where pressure jump passed (Fig. 9). On March 4, pressure disturbances exceeding the intensity criteria for a pressure jump and sea level oscillations exceeding 2–3 times the amplitude criteria for a meteotsunami were observed together in the B–E (33–36°N) latitude band (Fig. 9a, e). From 21:00 KST on April 5 and 03:00 KST on April 6, especially in B–C (35–37°N) latitude band, the pressure jumps were detected and the resultant sea level oscillations of 10–14 cm amplitude, was observed (Fig. 9b, f). On April 7, a low intensity pressure disturbance less than 0.3 hPa/10 min, was observed in the overall latitude band, and the pressure jump was concentrated only along the 36°N latitude, which is the B–C (35–37°N) latitude band boundary (Fig. 9c). At the time, the maximum amplitude of the sea level oscillations was only approximately 8 cm at EC (7) TG and GS (8) TG where the pressure jump passed (Fig. 9g). On April 10, the maximum amplitudes either exceeding or near the amplitude criteria for a meteotsunami were observed in the A–D (34–38°N) latitude band where the pressure jump propagated (Fig. 9d, h).

The amplitude of the high-frequency sea level oscillations was qualitatively correlated with the intensity of the pressure disturbance, but the degree of the amplification was significantly different depending on the event and space. The amplification of the sea level oscillations was needed to be confirmed quantitatively when the same intensity of the pressure disturbance occurs. Thus, the "generation coefficient (R)" was used (Šepić and Rabinovich 2014):

$$R^i_{\max} = A^i_{\max} / P^i_{\max} \tag{1}$$

which is parameterized by normalizing the maximum amplitude of the meteotsunami (A) by the maximum intensity of the pressure disturbance (P) in each latitude band (i). The generation coefficient makes it easier to identify the discrepancy, which indicates that the intensity of the pressure disturbance and the amplitude of the sea level oscillations are not always proportional. As a result, we were able to compare the degree of the amplified meteotsunami due to factors other than the intensity of the pressure disturbance for each event and latitude band.

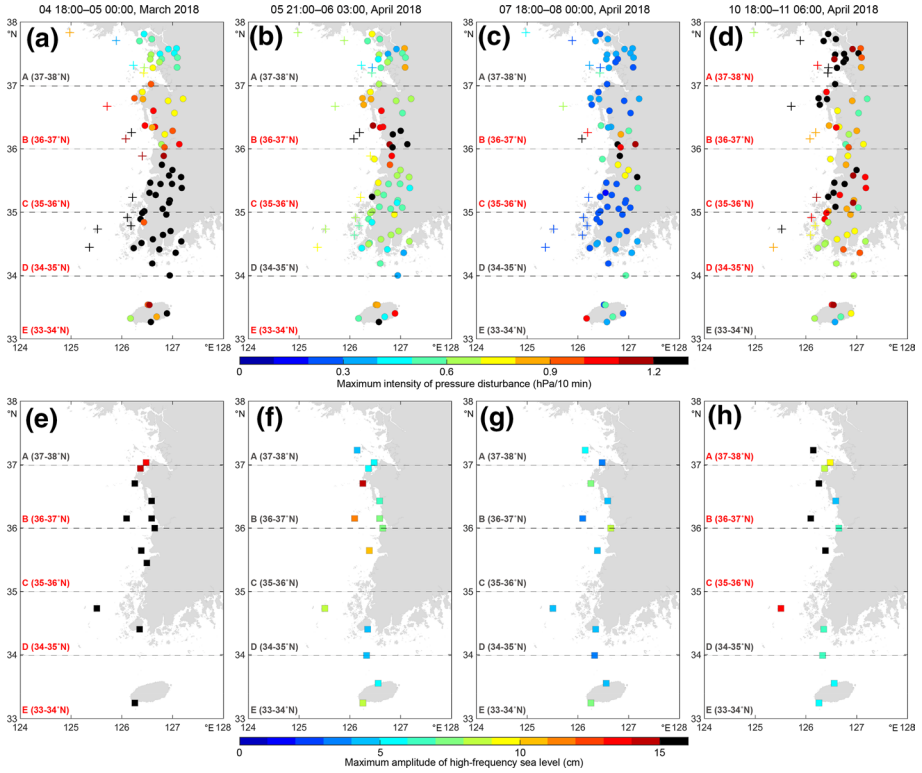


Fig. 9 Magnitude of the pressure disturbances and the sea level oscillations during the pressure jump events according to five latitude bands; A (37–38°N), B (36–37°N), C (35–36°N), D (34–35°N), and E (33–34°N): **a–d** the maximum intensity of the pressure disturbance at AWS; crosses and circles indicate AWS #1 and AWS #2, respectively; black crosses and circles mark AWS where the intensity criteria for a pressure jump (1.2 hPa/10 min) were exceeded; **e–f** the maximum amplitude of the high-frequency sea level oscillations at TG (squares); black squares mark TG where the amplitude criteria for a meteotsunami (15 cm) was exceeded

The event on March 4 of the four pressure jump events had the largest amplification of the meteotsunami amplitude versus the intensity of pressure disturbance, with the maximum generation coefficient of 18.9 and the mean generation coefficient of 11.2 (Table 1). The pressure jumps and meteotsunamis occurred most frequently in the B–C (35–37°N) latitude band regardless of the event (Fig. 9), but the mean generation coefficient for latitude band was the largest in A (37–38°N) latitude band (Table 1). Based on the rain rate, which is a proxy for the intensity of the pressure disturbance (Wertman et al. 2014), it can be inferred that the intensity of the pressure disturbance decreased sharply after passing through the land (Fig. 4). The B–C latitude band around a large bay will be relatively free from terrain effects independent of the direction from which the pressure jump propagated. Accordingly, it is presumed that during the pilot test, pressure disturbances exceeding the intensity criteria for a pressure jump were frequently detected in the B–C latitude band. In particular, except for the A (37–38°N) latitude band, the generation coefficient of the latitude band where the initial pressure jumps were detected was smaller than that of the other latitude band (Fig. 4, 5 and 6, Table 1). This was because the pressure disturbance that had relatively high intensity

Table 1 Generation coefficient (Šepić and Rabinovich 2014) according to the pressure jump events and latitude bands

	04 18:00–05 00:00 March 2018	05 21:00–06 03:00 April 2018	07 18:00–08 00:00 April 2018	10 18:00–11 06:00 April 2018	Mean
A (37–38°N)	12.1	6.6	12.0	15.3	11.5
B (36–37°N)	18.1	10.3	5.7	9.4	10.9
C (35–36°N)	18.9	7.9	6.2	8.4	10.4
D (34–35°N)	4.2	12.1	12.2	7.8	9.1
E (33–34°N)	2.9	4.3	7.2	5.8	5.1
Mean	11.2	8.2	8.7	9.3	–

tended to be detected in the latitude band where the initial pressure jump arrived before the pressure disturbance was attenuated in the propagation process.

Overall, there was a qualitative correlation between the intensity of the pressure disturbance and the sea level oscillations up to a certain intensity of the pressure disturbance. At higher intensities, the increase in the intensity of pressure disturbances did not necessarily lead to quantitative amplification of sea level oscillations. The A latitude band (37–38°N) can be considered a latitude band with a relatively large level of amplification caused by factors other than the intensity of the pressure disturbance.

4 Discussion

A real-time pressure disturbance monitoring system was operated in March and April 2018 by utilizing the existing observation system in the Yellow Sea. As a result, four pressure jump events were detected, and two of them exceed the criteria for a meteotsunami. Two questions about the practicality and accuracy of the observation system and monitoring system follow:

1. In the present observation system, was it possible to detect a pressure jump in advance and send a timely SMS before the resultant meteotsunami arrived?
2. When the pressure jump was detected in the monitoring system, was the meteotsunamis also generated?

For a timely meteotsunami warning by sending SMS #1 and SMS #2, the current observation system needs to address two problems: (i) It is difficult to have enough lead time more than 10 min for SMS #2. (ii) AWS #1 does not exist near Jeju Island in the E latitude band (33–34°N).

Not only is the distance from AWS #1 to AWS #2 large, but AWS #2 is primarily located near the coastline of the mainland, unlike the TG, making it difficult to provide enough evacuation time after sending SMS #2. Therefore, the installation of at least one sea-based pressure measurement (such as oceanographic buoys placed with pressure sensor) for each latitude, which will perform the role of AWS #1 by placing the buoys farther west from AWS #1, is necessary. Until the buoys are deployed, temporary modification of the criteria for sending SMS #2 is suggested because installing additional measurements

is time-consuming and expensive. Currently, a pressure jump is pre-detected at AWS #1, and then, SMS # 2 is sent when detecting the propagated pressure jump at AWS #2. As a temporary solution, the protocol of SMS #2 needs to be modified to send SMS #2 to the second detected AWS, no matter where the pressure jump is detected after AWS #1. The exceptional protocol of the monitoring system is not as fundamental as a solution as deploying the additional buoys, but it will provide some lead time for SMS #2.

Since there is no AWS #1 near Jeju Island, it is impossible to send any SMS to residents on the island when the pressure jump propagates toward Jeju Island intensively. It is necessary not only to install the buoys in the caution zone but also to apply an exceptional protocol of SMS #2 to Jeju Island. This is because the average depth of western Jeju island is approximately 90 m (Fig. 8), which may have faster shallow water wave speed than propagation speeds of pressure jumps ($Fr > 1.0$). Therefore, when the pressure jump arrives at the new buoys in the caution zone, SMS #2 should be sent directly to the residents in western Jeju Island to provide sufficient evacuation time.

Although it was a limited period, the accuracy of the monitoring system was determined by four cases detected by the test operation for two months from March to April 2018. When the accuracy is evaluated based on whether the detection of pressure jump-meteotsunami occurrences is matched for each case, the accuracy of the monitoring system is 50% (2/4). Also, it is possible to analyze the accuracy of the monitoring system in terms of whether the detection of pressure jump-meteotsunami occurrence was matched for each latitude band. In the monitoring system, the latitude band where the pressure jumps were detected and the latitude band where the maximum amplitude of the observed sea level oscillations exceeded the amplitude criteria for a meteotsunami are shown as red highlighted text in Fig. 9. As a result, the coincidence between the occurrence of pressure jumps and meteotsunamis in each latitude band is calculated as 70% (14/20).

During the pilot test of the monitoring system, the amplitude of the high-frequency sea level oscillations did not always exceed the criteria for a meteotsunami when the pressure jump was detected. To identify the exceptional cases, the maximum amplitude of the sea level oscillation was compared relative to the maximum intensity of the pressure disturbance for each latitude band, as shown in Fig. 10. According to the criteria for a pressure jump and a meteotsunami, the cases are divided into Group 1 (pressure jumps were not detected but meteotsunamis occurred), Group 2 (pressure jumps were detected and meteotsunamis also occurred), Group 3 (pressure jumps were not detected and meteotsunamis also did not occur), and Group 4 (pressure jumps were detected but meteotsunamis did not occur). Of the 20 cases, there were no false-negative cases in Group 1 and there were 14 cases in Group 2 and Group 3. This means that the intensity of the pressure disturbance must exceed the criteria for a pressure jump to generate meteotsunamis in the Yellow Sea. Therefore, the pressure jump criteria are considered to be reasonable. However, the remaining six false-positive cases were distributed in Group 4, in which pressure jumps were detected but meteotsunamis were not detected. The false-positive cases were mostly located near pressure disturbances with 1.2–1.4 hPa/10 min intensity. There are no false-negative cases in Group 1, even when the intensity criteria for a pressure jump are raised from 1.2 to 1.5 hPa/10 min. Accordingly, we plan to reduce the false-positive cases in the future by raising the intensity criteria for a pressure jump to 1.5 hPa/10 min. If the false-positive case is detected again after these modifications, it suggests that there can be other factors that dissipate the amplitude of the meteotsunamis.

In contrast, outlier cases in Group 2 appear to be cases where the meteotsunami amplitude was nonlinearly amplified by other factors as well as the intensity of the pressure disturbance. Since most TG are located in harbors or breakwaters, the amplitude of the

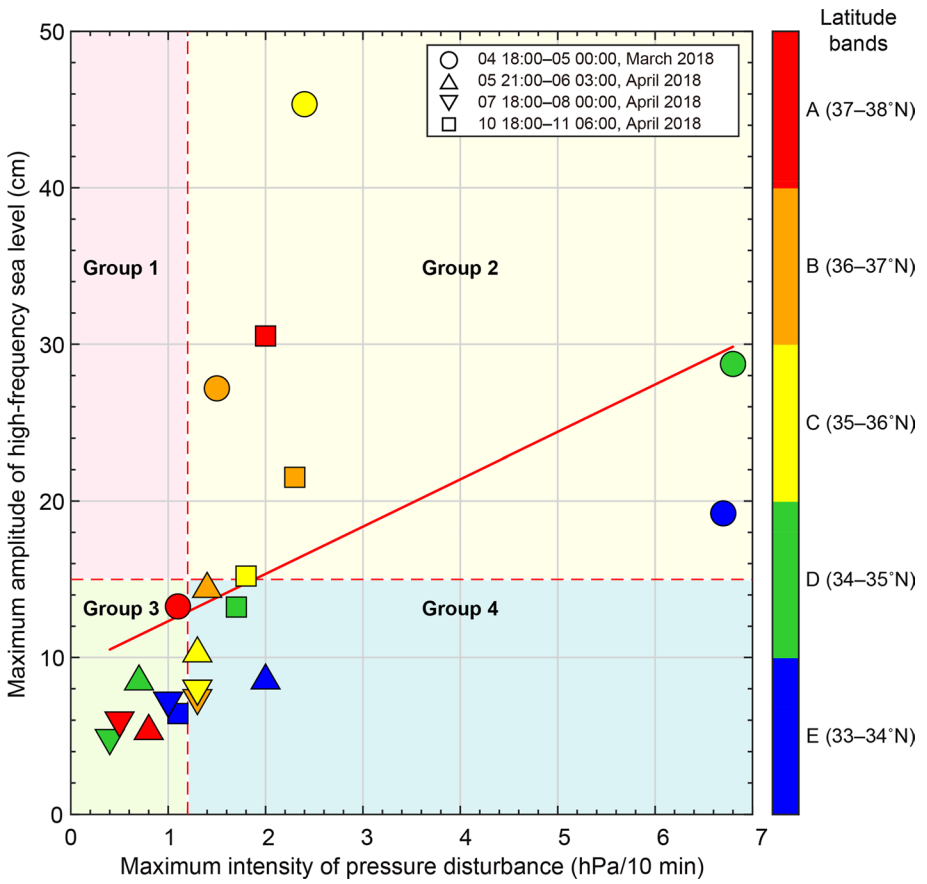


Fig. 10 Scatter diagram between the maximum intensity of the pressure disturbance and the maximum amplitude of the high-frequency sea level oscillations according to the pressure jump events and the latitude bands. The maximum value of each latitude band was determined as the representative value (the maximum) of the latitude band. Red dashed lines indicate the intensity criteria for a pressure jump (1.2 hPa/10 min) and a meteotsunami (15 cm) in the Yellow Sea, respectively. Red solid line shows a simple linear regression between the magnitude of the pressure disturbance and the sea level oscillations ($R^2 = 0.24$)

high-frequency sea level oscillations is inevitably affected by various amplification and attenuation as they propagate from the open ocean to the coast. The amplified amplitude observed inside a harbor may be produced by internal resonance (harbor resonance) after external resonance (Proudman, Greenspan, or shelf resonance) between pressure disturbance and the resultant sea level oscillations (Monseratt et al. 2006; Pattiaratchi and Wijeratne 2016). Strong wind disturbance exceeding 13 m/s at shallow water depth may increase high-frequency sea level oscillations (Linares et al. 2016). Vilibić et al. (2005) quantitatively suggested that a rise in wind speed by 30% could generate doubled maximum sea level oscillations through scenario modeling. The maximum height of meteotsunamis can also be affected by total water depth variation (Williams et al. 2020) and wave–tidal current interaction in shallow water in the Yellow Sea (Choi et al. 2014), which is a macrotidal region (tidal range is approximately 4 m between the neap and spring tide).

It is hard to consider additional amplification and attenuation factors in the current real-time monitoring system. Therefore, adjustments of the monitoring system were needed to reduce the false-positive cases in Group 4 as much as possible. We found the common characteristics of the pressure jump that are favorable to a meteotsunami other than the intensity of the pressure disturbance by comparing the events when pressure jumps were detected and meteotsunamis also occurred and the events when pressure jumps were detected but meteotsunamis did not occur. This approach was considered reasonable because the distribution of the exceptional cases in Group 2 and Group 4 was event-dependent, except for the D latitude band (34–35°N) case on April 10, 2018 (green square in Fig. 10).

In addition to the intensity of the pressure jump, another favorable condition for the generation of destructive meteotsunamis is the speed range of the pressure jump. The meteotsunami warning matrix can be determined to take into account that meteotsunami favorable conditions depend on the specific characteristics of the pressure jump such as intensity, direction, and speed range (Šepić and Vilibić 2011; Vilibić et al. 2016). Because there were only two cases in which pressure jumps were detected and meteotsunamis occurred, and the direction of the pressure jump events when meteotsunamis occurred were respectively different, we cannot find common points between the directions (Table 2). However, meteotsunamis were observed only above a certain minimum speed of the pressure jump, regardless of their propagation direction. The exceptional events where the pressure jumps were detected but meteotsunamis did not occur showed a pressure jump speed range of less than 10 m/s, while the meteotsunami events showed a pressure jump speed range of 12–36 m/s.

Through the common speed characteristics of four pressure jump events detected during the pilot test, the lower limit of the pressure jump speed favorable for meteotsunami development was 12 m/s. However, the upper limit could not be determined as a fixed speed because the speed range of the pressure disturbances was very broad and varied according to each propagation direction. Therefore, the upper limit of the pressure jump speed was assumed to be the maximum shallow water wave speed derived from the maximum depth

Table 2 Spatial characteristics and propagation pattern derived from the pilot test of the pressure jump monitoring system from March to April 2018

Pressure jump event	Spatial characteristics (rain rate, pressure jump)		Propagation pattern (pressure jump)		Propagation pattern (meteotsunami)	
	Spatial pattern	Latitude bands	Direction* (°)	Speed (m/s)	Direction* (°)	Speed (m/s)
04 18:00–05 00:00 March 2018	Linear or bow	B, C, D, E	241.9–279.6	20.3–36.3	234.1–283.4	9.8–23.0
05 21:00–06 03:00 April 2018	Cluster	B, C, E	260.3–276.8	5.3–9.8	–	–
07 18:00–08 00:00 April 2018	Local	B, C	319.0–320.1	8.7–10.4	–	–
10 18:00–11 06:00 April 2018	Linear	A, B, C, D	277.0–328.9	11.7–28.4	317.6–355.6	15.2–15.7

*Direction of the pressure jump and the meteotsunami is measured clockwise from the northward direction

between AWS #1 where the first pressure jump was detected and AWS #2 where the pressure jump was subsequently detected. The amplification of meteotsunami amplitude due to the Proudman resonance (Fr = 1) depends on the shallow water wave speed (c) in the area where the pressure jumps propagated (Monserrat et al. 2006). To reduce the false alarms reported from the monitoring system, it is necessary to modify not only the intensity criteria for a pressure jump but also the meteotsunami-prone pressure jump speed.

Currently, the monitoring system determines as a pressure jump that can generate a meteotsunami when the pressure jump propagated to a certain AWS #2 at a speed of at least 5 m/s after sending SMS #1. Since the pressure jump speed is calculated based on the maximum distance approximately 100 km between AWS #1 and AWS #2, the accuracy of the speed estimation is significantly reduced. Therefore, it is also required to modify the speed calculation method when determining the occurrence of a pressure jump.

Other than the common characteristics of the pressure jump, a specific spatial characteristic of rain clusters was also monitored during the pressure jumps detected on March 4–5 and April 10–11, 2018. Based on the storm structure classification associated with meteotsunamis generation (Bechle et al. 2015), the spatial patterns of the rain rate on the pressure jump events were categorized (Table 2). As a result, linear and bow type storm structures could create favorable conditions for the generation of pressure jumps and meteotsunamis in the Yellow Sea (Figs. 4c, d, 6e–h). This type of storm structure showed a more continuous and organized spatial pattern over the wide range of latitude bands than other types. Conversely, the unorganized distribution of the rain rate in two narrow latitude bands (35–37°N) was observed on April 5–6 and April 7–8, 2018, when the pressure jumps were detected (Fig. 5c, d). Since the event on April 7, 2018 did not correspond to any type of the storm structure classification, it was classified as a local type, featuring an extremely small spatial scale. Thus far, radar has been used to verify the propagation of pressure jumps, but radar and the pressure disturbance monitoring system will be operated simultaneously to monitor real-time spatial characteristics of pressure jump favorable to meteotsunami generation. It is expected that other characteristics of the rain rate such as intensity and spatial scale can also be collected later.

5 Summary and conclusions

As a result of the pilot test of the real-time pressure disturbance monitoring system from March to April 2018, we found that the accuracy of the current monitoring system was 50% due to two false-positive cases in which pressure jumps were detected and meteotsunamis did not occur. The monitoring system based on the air pressure measurements in the Yellow Sea was developed to prevent unexpected meteotsunami hazards through early detection of arrival time and propagation pattern of the pressure disturbance. Two levels of meteotsunami alerts (preliminary caution SMS and propagation warning SMS) were sent to mobile phones near AWS where pressure jumps arrived, and there were not any reported human casualties or economic damages during the pilot phase. Also, the monitoring system was useful for estimating the propagation of meteotsunamis by tracking the propagation pattern of the pressure disturbance that changes with time and space. Despite a limited number of events in a short period, of the four pressure jump events, the two pressure jump events in which meteotsunamis occurred have three common characteristics: (1) In all meteotsunami events including the reported events, the intensity of the pressure disturbance exceeds the minimum criteria for a pressure

jump (1.2 hPa/10 min). (2) The pressure jump speed exceeded at least 12 m/s when the pressure-forced sea level oscillations exceed the amplitude criteria for a meteotsunami (15 cm). Finally, (3) the linear and bow type of rain clusters, which are characterized as continuous and organized spatial distributions, appear to be favorable to meteotsunami generation.

The KMA is operating a different real-time monitoring system by focusing on frequent natural hazards in each season (e.g., rip current during summer season). Among the various systems, a potential meteotsunami monitoring system, which is operated temporarily in the spring season (March to April) when the frequent meteotsunami accident cases have been reported, has been suggested based on the meteotsunami favorable pressure disturbance conditions (Šepić et al. 2009; Šepić and Vilibić 2011; Vilibić et al. 2016). Thus far, there has been no real-time meteotsunami monitoring system operating with as many observation points (89 AWS). In this paper, this is not intended to claim that the current monitoring system is accurate, but to suggest the possibility of the pressure-based warning system by using the existing observation system. However, for faster and more accurate detection of meteotsunami, it is necessary to expand the observation system and to improve the monitoring system.

The reported problems of the observation and monitoring system during the pilot test are being corrected, and it is planned to be operated again in the spring of 2021. During the pilot test, the problems of the observation system were as follows: (1) limited SMS lead time, (2) absence of AWS #1 near Jeju Island, and (3) inability to track the temporal and spatial variability of the pressure disturbances in the open ocean. As a solution to these problems, we plan to utilize 11 additional mooring buoys that can cover the blank area of AWS and the open ocean. The buoys can monitor not only the pressure disturbances but also other meteorological variables such as winds, temperature, and wave height when meteotsunamis occur. Currently, five pre-installed buoys located near the west of AWS #1 can help to secure sufficient SMS lead time. The remaining six buoys are planned to be installed in the open ocean and west of Jeju Island by 2020. Furthermore, it is expected that the false-positive cases in the monitoring system can be reduced by (1) raising the intensity criteria for a pressure jump from 1.2 to 1.5 hPa/10 min, and (2) limiting the specific speed ranges of the pressure jump favorable to meteotsunami generation. The lower limit of the pressure jump speed was determined to be 12 m/s based on the common speed characteristics of the pressure jump events. The upper limit is assumed to be the maximum shallow water wave speed calculated from the maximum depth between the two AWS that could generate Proudman resonance.

Other than the adjustment of the monitoring system, it will be necessary to monitor real-time spatial patterns of the pressure jumps that are favorable for the generation of destructive meteotsunamis. Recently, the intensity of the pressure disturbance is correlated with the intensity of rain rate on radar (Wertman et al. 2014; Bechle et al. 2015); thus, it could be possible to track the evolution of pressure jump through radar in blank areas of AWS and mooring buoys. Based on the improvements in the observation and monitoring system in the Yellow Sea, it is possible to issue a more timely and reliable meteotsunami warning.

Funding This research was supported by Basic Science Research Program through the National Research Foundation of Korea (NRF) funded by the Ministry of Education (2019R1A6A3A13097301). Additionally, this research was a part of the project titled "Improvements of ocean prediction accuracy using numerical modeling and artificial intelligence technology," funded by the Ministry of Oceans and Fisheries, Korea.

Compliance with ethical standards

Conflict of interest The authors declare that they have no conflicts of interest.

References

Bechle AJ, Wu CH (2014) The lake Michigan meteotsunamis of 1954 revisited. Nat Hazards 74(1):155–177

Bechle AJ, Kristovich DAR, Wu CH (2015) Meteotsunami occurrences and causes in lake Michigan. J Geophys Res Ocean 120:8422–8438

Belušić D, Grisogono B, Bencetić Klaić Z (2007) Atmospheric origin of the devastating coupled air-sea event in the east Adriatic. J Geophys Res 112:D17111. https://doi.org/10.1029/2006JD008204

Candela J, Mazzola S, Sammari C, Limeburner R, Lozano CJ, Patti B, Bonnano A (1999) The "Mad Sea" phenomenon in the Strait of Sicily. J Phys Oceanogr 29:210–2231

Choi JY, Lee DY (2009) Analysis of small-scale atmospheric pressure jumps related to the generation of abnormal extreme waves at Boryeong. Ocean Polar Res 31(4):379–388

Choi BJ, Park YW, Kwon KM (2008) Generation and growth of long ocean waves along the west coast of Korea in March 2007. Ocean Polar Res 30(4):453–466

Choi BJ, Hwang C, Lee SH (2014) Meteotsunami-tide interactions and high-frequency sea level oscillations in the eastern Yellow Sea. J Geophys Res Ocean 119:6725–6742

Drago A (2009) Sea level variability and the 'Milghuba' seiche oscillations in the northern coast of Malta, Central Mediterranean. Phys Chem Earth 34:948–970

Eom HM, Seung YH, Woo SB, You SH (2012) Analysis of abnormal wave at the west coast on 31 March 2007. J Korean Soc Coast Ocean Eng 24(3):217–227

Garcies M, Gomis D, Monserrat S (1996) Pressure-forced seiches of large amplitude in inlets of the Balearic Islands. 2. Observational study. J Geophys Res 101:6453–6467

Gomis D, Monserrat S, Tintoré J (1993) Pressure-forced seiches of large amplitude in inlets of the Balearic Islands. J Geophys Res 98:14437–14445

Greenspan HP (1956) The generation of edge waves by moving pressure distributions. J Fluid Mech 1(6):574–592

Hibiya T, Kajiura K (1982) Origin of the Abiki phenomenon (a kind of seiche) in Nagasaki Bay. J Oceanogr Soc Jpn 38(3):172–182

Kim H, Kim YK, Woo SB, Kim MS (2014) Atmospheric analysis on the meteo-tsunami case occurred on 31 March 2007 at the Yellow Sea of South Korea. J Environ Sci Int 23(12):1999–2014

Kim MS, Kim H, Kim YK, You SH, Eom HM, Woo SB (2017) Determination of accurate arrival time of meteotsunami event in Yellow Sea. J Coast Res 79:149–153

Kim MS, Kim H, Eom HM, You SH, Woo SB (2019) Occurrence of hazardous meteotsunamis coupled with pressure disturbance traveling in the Yellow Sea, Korea. J Coast Res 91:71–75

Kim MS, Eom HM, Lim EP, Lee CK, You SH, Woo SB (2020) Method for detection of meteotsunami propagation in the Yellow Sea: reported cases. J Coast Res 95:1134–1139

Linares Á, Bechle AJ, Wu CH (2016) Characterization and assessment of the meteotsunami hazard in northern Lake Michigan. J Geophys Res Ocean 121(9):7141–7158

Marcos M, Monserrat S, Medina R, Orfila A, Olabarrieta M (2009) External forcing of meteorological tsunamis at the coast of the Balearic Islands. Phys Chem Earth 34:938–947

Monserrat S, Vilibić I, Rabinovich AB (2006) Meteotsunamis: atmospherically induced destructive ocean waves in the tsunami frequency band. Nat Hazards Earth Syst Sci 6:1035–1051

Ozsoy O, Haigh ID, Wadey MP, Nicholls RJ, Wells NC (2016) High-frequency sea level variations and implications for coastal flooding: a case study of the Solent, UK. Cont Shelf Res 122:1–13

Pattiaratchi C, Wijeratne EMS (2014) Observations of meteorological tsunamis along the south-west Australian coast. Nat Hazards 74:281–303

Pattiaratchi C, Wijeratne EMS (2016) Are meteotsunamis an underrated hazard? Philos Trans R Soc A Math Phys Eng Sci 373(2053):20140377. https://doi.org/10.1098/rsta.2014.0377

Pellikka H, Rauhala J, Kahma KK, Stipa T, Boman H, Kangas A (2014) Recent observations of meteotsunamis on the Finnish coast. Nat Hazards 74:197–215

Proudman J (1929) The effects on the sea of changes in atmospheric pressure. Geophys Suppl Mon Not R Astron Soc 2(4):197–209

Rabinovich AB (2009) Seiches and harbour oscillations. In: Kim YC (ed) Handbook of coastal and ocean engineering. World Scientific Publishing Co., Singapore, pp 193–236

Rabinovich AB, Monserrat S (1996) Meteorological tsunamis near the Balearic and Kuril Islands: descriptive and statistical analysis. Nat Hazards 13(1):55–90
Rabinovich AB, Monserrat S (1998) Generation of meteorological tsunamis (large amplitude seiches) near the Balearic and Kuril Islands. Nat Hazards 18(1):27–55
Šepić J, Vilibić I (2011) The development and implementation of a real-time meteotsunami warning network for the Adriatic Sea. Nat Hazards Earth Syst Sci 11:83–91
Šepić J, Rabinovich AB (2014) Meteotsunami in the Great Lakes and on the Atlantic coast of the United States generated by the "derecho" of June 29–30, 2012. Nat Hazards 74(1):75–107
Šepić J, Denis L, Vilibić I (2009) Real-time procedure for detection of a meteotsunami within an early tsunami warning system. Phys Chem Earth 34:1023–1031
Šepić J, Vilibić I, Strelec Mahović N (2012) Northern Adriatic meteorological tsunamis: observations, link to the atmosphere, and predictability. J Geophys Res 117:C02002. https://doi.org/10.1029/2011JC007608
Šepić J, Vilibić I, Fine I (2015a) Northern Adriatic meteorological tsunamis: assessment of their potential through ocean modeling experiments. J Geophys Res Ocean 120:2993–3010
Šepić J, Vilibić I, Rabinovich AB, Monserrat S (2015b) Widespread tsunami-like waves of 23–27 June in the Mediterranean and Black Seas generated by high-altitude atmospheric forcing. Sci Rep 5:11682. https://doi.org/10.1038/srep11682
Šepić J, Vilibić I, Monserrat S (2016) Quantifying the probability of meteotsunami occurrence from synoptic atmospheric patterns. Geophys Res Lett 43:10377–10384
Šepić J, Vilibić I, Rabinovich AB, Tinti S (2018) Meteotsunami ("Marrobbio") of 25–26 June 2014 on the Southwestern Coast of Sicily. Italy Pure Appl Geophys 175(4):1573–1593
Torrence C, Compo GP (1998) A practical guide to wavelet analysis. Bull Am Meteorol Soc 79(1):61–78
Vilibić I, Domijan N, Čupić S (2005) Wind versus air pressure seiche triggering in the Middle Adriatic coastal waters. J Mar Syst 57:189–200
Vilibić I, Šepić J, Rabinovich AB, Monserrat S (2016) Modern approaches in meteotsunami research and early warning. Front Mar Sci 3(57):1–7
Vilibić I, Šepić J, Dunić N, Sevault F, Monserrat S, Jordà G (2018) Proxy-based assessment of strength and frequency of meteotsunamis in future climate. Geophys Res Lett 45:10501–10508
Wertman CA, Yablonsky RM, Shen Y, Merrill J, Kincaid CR, Pockalny RA (2014) Mesoscale convective system surface pressure anomalies responsible for meteotsunamis along the U.S. East Coast on June 13th, 2013. Sci Rep 4:7143. https://doi.org/10.1038/srep07143
Williams DA, Horsburgh KJ, Schultz DM, Hughes CW (2020) Proudman resonance with tides, bathymetry and variable atmospheric forcings. Nat Hazards. https://doi.org/10.1007/s11069-020-03896-y

Publisher's Note Springer Nature remains neutral with regard to jurisdictional claims in published maps and institutional affiliations.